Final Draft

of the original manuscript

Shastri, H.; Mondal, A.; Dutta, K.; Dieringa, H.; Kumar, S.:

Microstructural correlation with tensile and creep properties of AZ91 alloy in three casting techniques.

In: Journal of Manufacturing Processes. Vol. 57 (2020) 566 - 573.

First published online by Elsevier: 17.07.2020

https://dx.doi.org/10.1016/j.jmapro.2020.07.010

Microstructural correlation with tensile and creep properties of AZ91 alloy in three casting techniques

Hrishikesh Shastri[a], A. K. Mondal[b,*], K. Dutta[a], H. Dieringa[c] and S. Kumar[d]

[a]Department of Metallurgical and Materials Engineering, National Institute of Technology, Rourkela-769008, India.

[b]Department of Metallurgical Engineering, Indian Institute of Technology (BHU) Varanasi, Varanasi - 221005, India.

[c]Magnesium Innovation Centre-MagIC, Institute for Materials Research, Helmholtz-Zentrum Geesthacht, 21502 Geesthacht, Germany.

[d]Department of Materials Engineering, Indian Institute of Science, Bangalore-560012, India.

Abstract

The relationships among microstructure, tensile and creep behaviour of the AZ91 Mg alloy produced by three different casting techniques have been investigated. All the as-cast alloys consist of primary Mg (α-Mg) and β-$Mg_{17}Al_{12}$ phases. The volume fraction of β-$Mg_{17}Al_{12}$ phase is the highest in the gravity casting (GC), intermediate in the squeeze-casting (SC) and the lowest in the high-pressure die-casting (HPDC). The best tensile properties are exhibited by the SC alloy at all the temperatures employed in the present investigation owing to the presence of negligible porosity and relatively finer grain size. Fracture surfaces of the broken tensile specimens reveal the quasi-cleavage fracture. The best and the worst creep resistance are exhibited by the SC and HPDC alloys respectively with the GC alloy exhibiting the intermediate creep resistance. The inferior creep resistance of the HPDC alloy is attributed to

*Corresponding author. Tel.: +91 542 236 9346; fax: +91 542 236 9478.

E-mail addresses: akmondal.met@iitbhu.ac.in (A. K. Mondal).

the presence of a higher amount of porosity that allows easy crack initiation and growth during creep tests. On the contrary, the negligible porosity and continuous network of eutectic phase contributes to the superior creep resistance of the SC alloy.

Keywords: AZ91 Mg alloy; Casting technique; Microstructure; Tensile; Creep

1. Introduction

Environmental concern and exhaustible reserves of fossil fuel demand for weight-saving to attain improved fuel efficiency in the automotive industry. In this regard, magnesium (Mg) alloys possessing high specific strength are the most promising structural materials for applications in aerospace and automotive industries. The production of wrought Mg alloys, in general, and especially AZ91 alloy, by plastic deformation (rolling, forging, extrusion) is challenging owing to the hexagonal close-packed (HCP) crystal structure and low stacking fault energy of Mg, and the presence of ample dendritic second phases in the microstructure resulting from the high Al content [1–5]. The problems like edge cracking in rolling as well as inadequate ductility during rolling, forging and extrusion cause a decline in the product quality and final yield of Mg alloys. Further, the processing by Equal Channel Angular Pressing (ECAP) involves removal of the pressed billet from the die for the next pass, re-heating and fitting it again in the die. Obtaining the desired microstructure in Mg alloys requires a lot of effort, and it is time-consuming, which makes it challenging for implementation at an industrial scale [6]. Contrary to rolling, forging, extrusion or ECAP, components are manufactured in a single operation in advanced casting methods with better homogeneity, lower energy consumption, almost no scrap and higher yield [3]. The Mg alloys possess better castability owing to excellent fluidity and low tendency to form hydrogen porosity compared to the metals like Al and Cu [7]. As a result, casting became the

dominant fabrication method for the components made of Mg alloys [8]. Thus, Mg alloys are primarily used in as-cast condition to fabricate intricate components, and the casting conditions or parameters (i.e., solidification rate, volume fraction and morphology of intermetallic phases, grain size, porosity, the degree of solute supersaturation etc) decide their properties.

The different methods available for casting Mg alloys are gravity casting (GC) (sand casting, permanent mold casting), die-casting (high-pressure, low-pressure, vacuum), squeeze-casting (SC), thixomolding, semi-solid metal casting, lost foam casting and ablation casting [9]. Among the various casting techniques available, gravity casting (GC) and high-pressure die-casting (HPDC) are widely used in automotive applications for the production of components such as instrument panels, steering assembly, wheels, seat frame, housings, console brackets, powertrain components etc [10]. As compared to GC, the HPDC is the most commonly employed for the production of Mg alloy components because of its high production rate and superior die-castability of Mg alloys. On the other hand, the GC is employed for various structural applications of automobile [9]. GC is a conventional casting process where the molten metal solidifies under the influence of gravity. In HPDC, molten metal is injected at high speed into the mold, and solidification occurs under high pressure. The solidification in HPDC is very rapid (varies from milliseconds to a few seconds) and yields a net-shaped component. The semi-solid metal casting, squeeze-casting, lost foam casting and ablation casting are considered to be the emerging casting processes. Among these processes, recently, squeeze-casting (SC) gained popularity owing to the superior properties exhibited by the castings produced by this route [9,11]. In SC, the rate of molten metal pouring is relatively slower, continuous and solidification takes place under high pressure that ensures negligible porosity in the casting. The governing reason for lower porosity in the SC than the

HPDC is that the former takes longer time for solidification and lower velocity of die filling than the latter ensuring less air entrapment. Thus, there are several casting techniques available, in general. However, in the present investigation, we have concentrated on the casting techniques that are most commonly employed for the production of Mg alloys (GC and HPDC). We have also considered the SC as it is the most promising among the emerging casting processes.

The high-temperature automobile powertrain applications, such as, valve cover, transmissions and engine blocks [9,12] demand superior elevated temperature strength along with good creep resistance of Mg alloys. Therefore, it is essential to investigate the high temperature tensile as well as creep properties of the alloys targeted for automobile applications. The tensile properties evaluated at ambient temperature are used as a benchmark. Gutman et al. [13] studied the influence of casting parameters on creep and strength of the AZ91D alloy fabricated by permanent mold casting as well as die-casting and reported a better creep resistance in the permanent mold cast alloy due to β-$Mg_{17}Al_{12}$ phase precipitation. In the die-cast alloy, the creep resistance was controlled by the presence of micro and macro porosities. The variation in tensile properties of the AZ91 alloy synthesized by sand-casting with varying solidification rate was reported by Caceres et al. [14]. Dargusch et al. [15] investigated the effect of varying section thicknesses of a HPDC AZ91 alloy and concluded that the mechanical properties at elevated temperature improved as section thickness was decreased. Han et al. [16] reported an increase in creep resistance of the AC52 alloy with increased cooling rate. Zhu et al. [17] too studied the effect of varying cooling rate using chill at one end of the cast plate on the fraction of β-$Mg_{17}Al_{12}$ phase in the sand-cast AZ91 alloy. They observed that the fraction of eutectic β-$Mg_{17}Al_{12}$ phase decreased and the discontinuous β-$Mg_{17}Al_{12}$ phase increased towards the chill end of the casting. However, they did not

investigate the mechanical properties of the alloy. The superior mechanical properties, including creep behaviour, were reported in the die-cast Mg-3Sm-0.5Zn-0.4Zr (wt.%) alloy by Zheng et al. [18]. Ferri et al. [19] also noticed an improvement in the strength of the ZAXLa05413 alloy subjected to unidirectional cooling as compared to the isothermal cooling. Kim et al. [20] reported that the Mg-4Al-2Sn alloy in die-cast condition exhibited better creep resistance than that in GC condition. Bai et al. [21] also observed the difference in tensile and creep properties with varying casting conditions in the Mg-4Al-(1-4) La alloy. Mondal et al. [22] reported better creep resistance of the HPDC MRI230D alloy as compared to the GC alloy. Zhao et al. [23] investigated the effect of varying squeeze pressure during SC on the microstructure of GZ151K Mg alloy. They observed finer grain size and reduced volume fraction of β_1 precipitates in the SC alloy compared to the GC alloy. Patel et al. [24] too reported refined dendritic and eutectic structure leading to minimum wear rate in the SC alloy as compared to the GC alloy.

The above-mentioned review evidenced that the mechanical properties of Mg alloys differ significantly with cooling rates and casting routes employed to fabricate the alloys. Although preliminary results exist on the effect of cooling rates and the role of conventional casting routes on mechanical properties of the AZ91 alloy, these results do not precisely correlate the situation prevailing in advanced casting like SC. Consequently, it is worth correlating microstructure and mechanical properties of the AZ91 alloy fabricated by three different casting techniques to ascertain the most suitable casting route for economic and large-scale production.

2. Experimental procedure

The as-received material was the commercial AZ91 alloy ingots, and these were gravity cast. The GC alloy in the present investigation was produced by re-melting these ingots in an electrical resistance furnace. The re-melting of the ingots was carried out in order to remove any ambiguity. Melting of the alloy was carried out at 993 K. A mixture of SF_6 (0.5 vol%) and Ar (99.5 vol%) was purged during the whole process to protect the melt from oxidation. The melt was poured at 973 K into a steel mold (50 mm diameter and 250 mm height) preheated to 483 K, and allowed to cool to room temperature. The same melting practice was employed to fabricate the SC alloy. Solidification took place in around 60 s under 120 MPa. The HPDC alloy was cast in a cold chamber high-pressure die-casting machine (FRECH DAK 450-54RC) in the form of a cylindrical rod of 19 mm diameter and 179 mm length. The melt temperature and the pressure during solidification were maintained at 963 K and 300 bar, respectively. The densities of the three alloys were measured using Archimedes' principle. The porosity content of the alloys was calculated by the following formula.

$$\%Porosity = \left(\frac{\rho_t - \rho_e}{\rho_t}\right) \times 100\%$$

Where ρ_t and ρ_e are the values of theoretical and experimentally calculated densities respectively. The value of theoretical density (ρ_t) of the AZ91 alloy is 1.810 gm/cm^3.

The microstructures of the alloys were observed using an optical microscope (ZEISS AxioVision I10) and scanning electron microscope (SEM) (FEI Quanta 200) equipped with energy-dispersive X-ray spectroscopy (EDS) (Oxford Instruments). A transmission electron microscope (TEM) (Model: JEOL JEM 2100) with EDS (Model: OXFORD INCA X-SIGHT) equipped to it was employed to take the micrographs from the as-cast as well as creep tested squeeze-cast (SC) AZ91 alloy. The specimens for TEM observation were arranged by punching several discs of 3 mm diameter followed by mechanical thinning to 1

μm thickness. Finally, the foils were subjected to ion milling (Model: Gatan Duo Mill 600). The grain size, the volume fraction of phases and precipitates, and secondary dendrite arm spacing (SDAS) were quantified with the help of image analyzer. The phases present in the alloys were identified by an X-ray diffractometer (XRD) (Rigaku Japan/Ultima-IV) employing CuKα (λ = 1.541 Å) radiation. A scan rate of 2º/min in the scan range (2Θ) of 10-90º with a step size of 0.05 was employed. The operating voltage and current of the XRD were 40 kV and 40 mA respectively.

The tensile specimens were tested following the ASTM E8M-03 standard in a universal testing machine (INSTRON 5967) at ambient, 423 K and 473 K temperature. The tensile specimens of 4 mm diameter and 20 mm gauge length were tested employing a strain rate of 10^{-3} s^{-1}. The test at each parameter was repeated at least three times, and the average value taken from the tests are reported here as tensile properties. The creep tests were carried out using specimens of 6 mm diameter and 15 mm length in a creep setup (ATS 2330) under compression at 70 MPa and 423 K. Fracture surfaces of the tensile and creep tested specimens were observed under SEM.

3. Results and discussion

3.1 As-cast microstructure

Fig. 1 shows the XRD patterns obtained from the AZ91 alloy in three different casting conditions. The alloy in all three casting conditions consists of α-Mg and β-$Mg_{17}Al_{12}$ phases. The intensity of the peak conforming to β-$Mg_{17}Al_{12}$ phase is the highest and the lowest in the GC and HPDC alloys, respectively. Thus, the volume fraction of the low melting point β-$Mg_{17}Al_{12}$ phase is the highest and the lowest in the GC and HPDC alloys, respectively.

The optical micrographs of the AZ91 alloy in all three casting conditions are shown in Fig. 2. The microstructures of all the alloys consist of α-Mg phase and bright β-$Mg_{17}Al_{12}$ phase present along grain boundaries and triple points. The alloy in all the casting conditions consists of polygonal grains. The average grain sizes are 70.26 ± 4.53, 41.20 ± 3.85 and 26.44 ± 1.96 μm for the GC, SC and HPDC alloys respectively. Thus, the HPDC alloy exhibits relatively finer grain size than that of the GC and SC alloys. The slow cooling rate associated with the GC allowed ample time for grain growth, whereas, in the other two alloys, the cooling rate was much higher, resulting in relatively finer grain sizes. The high degree of undercooling associated with the faster cooling rate following HPDC facilitated the formation of a large number of nuclei in the liquid Mg alloy. However, the slow diffusion rate at the corresponding temperature leading to low growth rate resulted in microstructural refinement [25]. The SDAS values are 68.01 ± 6.53, 35.50 ± 5.09 and 31.99 ± 4.67 μm for the GC, SC and HPDC alloys. The SDAS decreases with increase in solidification rate.

The SEM micrographs of the AZ91 alloy in all three casting conditions are shown in Fig. 3. The EDS analysis carried out in the grain interior of the GC alloy shown in Fig. 3(a) exhibits an average composition of 94.86 ± 0.61 Mg, 4.72 ± 0.44 Al, 0.29 ± 0.11 Zn and 0.13 ± 0.05 Mn (at.%), which corresponds to α-Mg. Similarly, the EDS analysis of the bright lamellar phase present along grain boundaries and triple points indicates an average composition of 61.44 ± 5.6 Mg and 41.74 ± 4.5 Al (at.%). Therefore, the grain boundary phase is β-$Mg_{17}Al_{12}$ phase as marked by the arrows in Fig. 3. A few globular Al-Mn rich particles (shown by arrows in Fig. 3(b)) are also observed and EDS analysis exhibits an average composition of 44.02 ± 4.6 Al, 24.28 ± 2.1 Mn and 31.41 ± 1.4 Mg (at.%). EDS analysis was also carried out on the other two alloys revealing the grain interior as α-Mg; the bright phase present along grain boundaries and triple points as β-$Mg_{17}Al_{12}$ phase; and a few Al-Mn-rich phase. Thus,

the existence of the same phases, i.e., α-Mg, β-$Mg_{17}Al_{12}$ and Al-Mn-rich phases in the AZ91 alloy in all three casting conditions are confirmed.

The GC, SC and HPDC alloys differed much on the following grounds. The calculated average volume fraction of the grain boundary phase in the GC alloy (i.e., 17.88 ± 0.24%) is higher than that observed in the SC (i.e., 8.16 ± 3.15%) and HPDC (i.e., 7.59 ± 0.45%) alloys. Thus, the fraction of β-$Mg_{17}Al_{12}$ phase decreases with increase in solidification rate owing to the fact, that high cooling rate does not allow Al in the α-Mg matrix to precipitate. Therefore, it forms a Mg-Al-Zn supersaturated solid solution during solidification. Barbagallo et al. [26] too observed a decreased volume fraction of the grain boundary β-$Mg_{17}Al_{12}$ phase with an increase in cooling rate in the AZ91 alloy. Another noteworthy dissimilarity observed is the difference in morphology of the eutectic β-$Mg_{17}Al_{12}$ phase, which is quite sensitive to small variations in cooling conditions and alloy content. The observed eutectic phase is partially divorced, coarse and discontinuous in the GC alloy. On the other hand, it is partially divorced and formed a continuous network along the grain boundaries and the triple points in the SC alloy; fully divorced and discontinuous in the HPDC alloy. In addition, the GC alloy exhibits a wider eutectic structure than that of the SC and HPDC alloys. The former alloy allows sufficient time for the growth of the precipitates, thereby widening the structure of the eutectic phase. Nave et al. [27] too reported similar microstructural characteristics, i.e., the β-$Mg_{17}Al_{12}$ phase was partially divorced in the GC Mg-9Al alloy. The reason behind the formation of divorced eutectic in Mg alloys is well explained in the literature [27,28]. A binary Mg-Al alloy of eutectic composition (i.e., Mg-33Al (wt.%)) typically solidifies with a regular lamellar or fibrous morphology comprising of α-Mg and β-$Mg_{17}Al_{12}$ phases depending on cooling rates. The tendency to form divorced eutectic is increased with an increase in the volume fraction of the primary phase resulting

from low Al content in the alloy. Thus, the hypoeutectic Mg alloy with low solute concentration generally exhibits divorced or partially divorced eutectic microstructures [28]. The tendency to form divorced eutectic was enhanced by the addition of a small amount of Zn that strongly segregated into the liquid as compared to Al. Further, this tendency increased with the increase in cooling rate. In the alloys, the α-Mg phase appeared as light grey and it gradually became darker towards grain boundaries owing to the higher concentration of Al and Zn that was detected by EDS analyses. A similar observation has been made in the GC AZ91 alloy by Nave et al. as well [27].

To assess the segregation tendency of Al, the concentration of Al interior of α-Mg near grain boundary was measured using EDS, and the values are 6.29 ± 1.11, 9.39 ± 0.36 and 14.62 ± 5.13 (at.%) in GC, SC and HPDC alloys. Thus, the Al concentration in the interior of α-Mg in the alloy in three different casting conditions is not the same, and it is the highest in the HPDC alloy and the lowest in the GC alloy, as expected. The rapid cooling rate associated with the HPDC process was responsible for the formation of a supersaturated solid solution of Al in α-Mg grains. Consequently, the amount of Al available for β-$Mg_{17}Al_{12}$ phase formation was lower and therefore, the final volume fraction of β-$Mg_{17}Al_{12}$ phase in the HPDC alloy at the end of solidification is relatively less.

Another notable distinction witnessed is the difference in porosity content. The density values measured by Archimedes' principle of the GC, SC and HPDC alloys are 1.790, 1.807 and 1.722 gm/cm^3, respectively. The corresponding values of the porosity of the GC, SC and HPDC alloys are 1.105, 0.166 and 4.862%, respectively. Thus, the porosity content is the highest in the HPDC alloy (marked by arrows in Fig. 2(c)), and it is insignificant in the SC alloy, with the GC alloy exhibiting the intermediate porosity. The higher porosity observed in

the HPDC alloy is attributed to the difference in liquid metal temperature (i.e., casting temperature), die (mold) temperature, metal injection rate into the die as well as casting conditions including the process of melt preparation and the possibility of air entrainment during metal injection into the die [29]. Besides, the distinct difference in solidification pressure among the three casting technologies might also influence the microstructures of the alloys.

3.2 Tensile behaviour

Fig. 4(a) shows the tensile properties of the AZ91 alloy in different casting conditions tested at ambient temperature. It is observed that the casting condition significantly influenced the tensile properties of the AZ91 alloy. The 0.2% proof stress (YS) and ultimate tensile strength (UTS) are the lowest for the GC alloy, intermediate for the HPDC alloy, and the highest for the SC alloy. The ductility (% Elongation) of the HPDC alloy is the lowest; for SC alloy it is highest and for GC alloy intermediate. The YS and UTS values decrease, and correspondingly, the ductility increases for the alloys in all casting conditions when tested at 423 K and 473 K, as shown in Fig. 4(b&c). The ductility of the GC, SC and HPDC alloys increases by 21.0, 14.7 and 15.7% at 423 K; and 26.3, 25.0 and 20.6% at 473 K, respectively. The reason behind improved ductility of all the alloys at elevated temperature is the operation of extra slip systems [30]. The best tensile properties are observed in the SC alloy at all the temperature levels. It exhibits 3.4 ± 0.17, 3.9 ± 0.20 and 4.1 ± 0.21% ductility with corresponding UTS of 140 ± 7.0, 132 ± 6.6 and 120 ± 7.0 MPa at ambient, 423 K and 473 K temperature, respectively. The improved tensile behaviour of the SC alloy could be associated with relatively finer grain size and negligible porosity present in the casting.

The GC alloy revealed relatively low YS, UTS, and ductility due to the presence of higher volume fraction of brittle β-$Mg_{17}Al_{12}$ phase rendering the alloy brittle. The coarse grain size also contributed to the inferior tensile properties of the GC alloy. The relatively poor tensile properties with the lowest value of ductility of the HPDC alloy might be due to structural inhomogeneity comprising of micro porosities present in the casting. Wei et al. [31] concluded the detrimental effect of voids formed by air entrapment during HPDC on the mechanical properties of the AZ91D alloy. Dúl et al. [32] too, in their investigation observed inhomogeneity in the internal structure of the HPDC alloy. The existing pores, where the lattice of the alloy was significantly distorted, acted as stress raisers and crack initiated there. Once the crack formed, it connected the neighbouring pores and was thus, allowing an easy path for rapid crack propagation.

Fig. 5(a-c) shows the micrographs of fracture surfaces of tensile specimens of the GC, SC and HPDC alloys tested at ambient temperature. Features revealed are cracks (indicated by A), porosity (B), quasi-cleavage plane (C), steps (D), plastic deformation zone (E), shallow dimples (F) and these are marked in the micrographs. The micrograph of the GC alloy exhibits the presence of various cleavage steps. A small deformation zone is also present. Multiple cracks are observed in the micrograph of the HPDC alloy, and these cracks initiated from the sharp edges of the pores. A few quasi-cleavage planes (C) with steps of various sizes are also observed. These are the characteristics of brittle intergranular cleavage fracture that took place along grain boundaries. Owing to the limited number of slip systems operated at ambient temperature dislocation movement in the neighbouring grains was restricted leading to the reduced ductility of all the alloys. The quasi-cleavage fracture was the failure mode in the SC alloy in which the cracks initiated and propagated locally forming a shallow dimple like morphology on the fracture surface. The presence of second phases and their

nature played an important role in the origin of micro-cracks. During tensile test micro-cracks might have initiated at the interfaces of the brittle eutectic present along the grain boundaries, thus, rendering the alloy brittle. Patel et al. [33] also observed secondary cracks on the fracture surface propagated along the interface of the eutectic phase in the AZ91D alloy. The presence of a relatively higher number of shallow dimples and plastic deformation zones on the fracture surface of the SC alloy evidenced its higher ductility. Fracture surfaces of all the specimens of the alloys tested at 423 K and 473 K exhibited quasi-cleavage fracture as well. Mg alloy generally exhibits limited ductility owing to limited slip systems operating at ambient temperature. However, beyond 498 K, the ductility of Mg alloy enhances owing to activation of additional slip systems containing prismatic and pyramidal planes along which cross-slip takes place [30]. The testing temperatures (i.e., 423 K and 473 K) employed were below 498 K, and accordingly, additional slip systems were not completely activated, which resulted in less improvement in ductility.

3.3 Creep behaviour

The characteristic creep curves of the AZ91 alloy in GC, SC and HPDC conditions tested at 70 MPa and 423 K are shown in Fig. 6(a). Different cooling rates associated with the GC, SC and HPDC alloys resulted in different creep characteristics. All the curves display a distinct primary creep followed by a secondary creep. The creep rate was calculated from the steady-state part of the strain vs. time curves, as shown in Fig. 6(b). The GC, SC and HPDC alloys exhibit a creep rate of 7.26×10^{-8}, 1.60×10^{-8} and 9.56×10^{-8} s^{-1} respectively. The creep rate is the highest in the HPDC, intermediate in the GC and the lowest in the SC alloys. The creep rate of the HPDC and GC alloys; GC and SC alloys; HPDC and SC alloys varies by a factor of 1.32, 5.97 and 4.53, respectively. Thus, the casting routes significantly affected the creep behaviour of the AZ91 alloy.

The observed differences in creep behaviour amongst the GC, SC, and HPDC alloys are attributed to several reasons. Different cooling conditions prevailing during castings resulted in varied microstructural features leading to the variation in creep behaviour. The difference in amount and morphology of the β-$Mg_{17}Al_{12}$ phase present along grain boundaries of the GC, SC and HPDC alloys resulted in the variation. Mondal et al. [22] investigated creep behaviour of the MRI230D alloy in the temperature range of 448-473 K and stress range of 60-120 MPa and concluded that the creep mechanism was dislocation creep. Nami et al. [34] too reported dislocation creep as the creep mechanism in the MRI153 alloy in the temperature range of 425-490 K and normalized stress range of 0.025-0.04. Spigarelli et al. [35] reviewed the literature on creep behaviour of the AZ91 alloy and concluded that the dislocation creep as the operating creep mechanism in the alloy. Thus, it is speculated based on the review of the literature on creep behaviour of Mg alloys, and especially of AZ91 alloy, that dislocation creep is the proposed creep mechanism in the present alloy in all three casting conditions at the stress and temperature level employed. The dislocation creep is generally observed at relatively low temperature and high applied stress $\left(10^{-4} < \frac{\sigma}{G} < 10^{-2}\right)$ [36]. The process of dislocation creep comprises the movement of dislocations that overcome obstacles using thermally activated mechanisms, such as, diffusion of vacancies and interstitials. Creep resistance increases if the dislocation glide or dislocation climb faces hindrance on the basal and non-basal planes leading to increased work hardening. At elevated temperature, if a gliding dislocation is stopped by an obstacle, a small upward or downward movement by climb might allow the dislocation to overcome the obstacle. Once the dislocation is free to move, it again encounters another obstacle and thus, the entire process is repeated. The dislocation glide produces the strain in the alloy, however, the climb controls the velocity.

Figure 7(a-c) shows the bright-field TEM micrographs taken from the SC AZ91 alloy as a representative picture for all the alloys. Figure 7(a) depicts the image in as-cast condition i.e., prior to the creep test. The micrograph demonstrates the presence of primary Mg solid solution (α-Mg) and β-$Mg_{17}Al_{12}$ phase, as expected. The entire micrograph is almost free from dislocations as the alloy was not subjected to creep deformation. Figure 7(b&c) presents the micrographs of the same SC alloy creep tested at 70 MPa and 423 K for 50 h. The presence of dislocations is noticed in the solid solution matrix, as revealed in Fig. 7(b). Figure 7(c) illustrates the interaction of the dislocations with the secondary β-$Mg_{17}Al_{12}$ phase. The presence of the β-$Mg_{17}Al_{12}$ phase restricted the movement of dislocations during the progress of the creep deformation causing dislocations to pile-up around it. It is also evident that few dislocations were formed in the interior of the secondary phase itself. The interaction among dislocations restricted the movement of dislocations causing work hardening of the alloy. Thus, the presence of the dislocations evidenced the dislocation creep mechanism. The presence of discontinuous β-$Mg_{17}Al_{12}$ phase in the HPDC alloy could not effectively provide an obstacle to dislocation motion. The SEM micrograph of the HPDC alloy creep tested at a stress of 70 MPa and temperature of 423 K is shown in Fig. 8. The existing porosities in the alloy joined together, providing an easy path for crack initiation and growth during the creep test.

A similar observation was also made by Mondal et al. [22] on the creep tested die-cast MRI230D alloy. Therefore, the higher porosity content of the HPDC alloy deteriorated its creep resistance. Thus, the extent of porosity played a crucial role in the creep behaviour of the HPDC alloy, which has been verified by Gutman et al. [13,29] as well. They observed that the minimum creep rate under the comparable condition increased considerably with an increase in porosity. As a consequence, easy crack initiation and growth during the creep test

took place reducing creep performance of the HPDC alloy. On the contrary, the presence of negligible porosity and continuous network of eutectic phase in the SC alloy contributed to its superior creep resistance. Amberger et al. [37] too concluded that the continuous and interconnected network of the intermetallic phase enhanced creep resistance in the modified AZ91 and MRI230D alloys. The intermediate creep performance exhibited by the GC alloy is attributed to the presence of relatively lesser porosity as well as coarser and discontinuous eutectic phase. The creep resistance of the GC alloy is superior to that of the HPDC alloy owing to the relatively lower porosity in the former alloy. On the other hand, it is slightly inferior as compared to that of the SC alloy due to the presence of coarser and discontinuous eutectic phase. The coarse and discontinuous eutectic phase contributed negatively to creep resistance due to lower pinning of dislocations. Kim et al. [20] also concluded that coarse eutectic phase favoured the formation of cracks allowing easy dislocation movement.

4. Conclusions

The following conclusions are drawn from the present investigation.

i. The AZ91 alloy in all the three casting conditions consists of α-Mg and β-$Mg_{17}Al_{12}$ phases. The volume fraction of the β-$Mg_{17}Al_{12}$ phase was the highest in the GC alloy, intermediate in the SC alloy, and the lowest in the HPDC alloy. The morphology of the eutectic was partially divorced, coarse and discontinuous in the GC alloy; partially divorced and continuous in the SC alloy, and fully divorced and discontinuous in the HPDC alloy.

ii. The best tensile properties were exhibited by the SC alloy owing to the presence of negligible porosity and finer grain size.

iii. The best and the worst creep resistance were exhibited by the SC and HPDC alloys with the GC alloy exhibiting the intermediate creep resistance. The poor creep

resistance of the HPDC alloy was attributed to the higher porosity that allowed an easy crack initiation and growth during creep. The presence of negligible porosity and continuous network of eutectic phase contributed to superior creep resistance of the SC alloy.

Acknowledgements

The authors gratefully acknowledge the support extended by the NRC-M at the Department of Materials Engineering, Indian Institute of Science, Bangalore.

References

[1] Chen B, Lin D, Jin L, Zeng X, Lu C. Equal-channel angular pressing of magnesium alloy AZ91 and its effects on microstructure and mechanical properties. Mater Sci Eng A 2008;483–484:113–6. https://doi.org/10.1016/j.msea.2006.10.199.

[2] Ebrahimi GR, Maldar AR, Ebrahimi R, Davoodi A. The effect of homogenization on microstructure and hot ductility behaviour of AZ91 magnesium alloy. Met Mater 2010;48:277–84. https://doi.org/10.4149/km_2010_5_277.

[3] Ghomashchi MR, Vikhrov A. Squeeze casting: an overview. J Mater Process Technol 2000;101:1–9. https://doi.org/10.1016/S0924-0136(99)00291-5.

[4] Kanayo KA, Okotete EA. Enhancing plastic deformability of Mg and its alloys — A review of traditional and nascent developments. J Magnes Alloy 2017;5:460–75. https://doi.org/10.1016/j.jma.2017.11.001.

[5] Xu Q, Ma A, Li Y, Sun J, Yuan Y, Jiang J, et al. Microstructure evolution of AZ91 alloy processed by a combination method of equal channel angular pressing and rolling. J Magnes Alloy 2020;8:192–8. https://doi.org/10.1016/j.jma.2019.05.012.

[6] Xu Q, Ma A, Li Y, Saleh B, Yuan Y, Jiang J, et al. Enhancement of Mechanical Properties and Rolling Formability in AZ91 Alloy by RD-ECAP Processing. Materials (Basel) 2019;12:3503. https://doi.org/10.3390/ma12213503.

[7] Luo AA, Sadayappan K. Technology for Magnesium Castings. Am Foundry Soc Schaumburg, 2011:29–47.

[8] Avedesian MM, Baker H, editors. Magnesium and Magnesium Alloys. ASM International; 1999.

[9] Luo AA. Magnesium casting technology for structural applications. J Magnes Alloy 2013;1:2–22. https://doi.org/10.1016/j.jma.2013.02.002.

[10] Luo AA. Materials Comparison and Potential Applications of Magnesium in Automobiles. In: Kaplan HI, Hryn JN, Clow BB, editors. Magnes. Technol., The Minerals, Metals & Materials Society; 2000, p. 88–98. https://doi.org/10.1002/9781118808962.ch15.

[11] Bankoti AKS, Mondal AK, Kumar S, Ray BC. Individual and combined additions of calcium and antimony on microstructure and mechanical properties of squeeze-cast AZ91D magnesium alloy. Mater Sci Eng A 2015;626:186–94. https://doi.org/10.1016/j.msea.2014.12.068.

[12] Gupta M, Sharon NML. Magnesium Alloys. In: Gupta M, Sharon NML, editors. Magnesium, Magnes. Alloy. Magnes. Compos., John Wiley & Sons, Inc.; 2011, p. 39–85. https://doi.org/doi:10.1002/9780470905098.ch3.

[13] Gutman EM, Unigovski Y, Levkovich M, Koren Z, Aghion E, Dangur M. Influence of technological parameters of permanent mold casting and die casting on creep and strength of Mg alloy AZ91D. Mater Sci Eng A 1997;234–236:880–3. https://doi.org/10.1016/S0921-5093(97)00363-8.

[14] Cáceres CH, Davidson CJ, Griffiths JR, Newton CL. Effects of solidification rate and ageing on the microstructure and mechanical properties of AZ91 alloy. Mater Sci Eng A 2002;325:344–55. https://doi.org/10.1016/S0921-5093(01)01467-8.

[15] Dargusch MS, Easton MA, Zhu SM, Wang G. Elevated temperature mechanical properties and microstructures of high pressure die cast magnesium AZ91 alloy cast with different section thicknesses. Mater Sci Eng A 2009;523:282–8. https://doi.org/10.1016/j.msea.2009.06.015.

[16] Han L, Northwood DO, Nie X, Hu H. The effect of cooling rates on the refinement of microstructure and the nanoscale indentation creep behavior of Mg–Al–Ca alloy.

Mater Sci Eng A 2009;512:58–66. https://doi.org/10.1016/j.msea.2009.01.068.

[17] Zhu T, Chen ZW, Gao W. Effect of cooling conditions during casting on fraction of β-$Mg_{17}Al_{12}$ in Mg-9Al-1Zn cast alloy. J Alloys Compd 2010;501:291–6. https://doi.org/10.1016/j.jallcom.2010.04.090.

[18] Zheng J, Wang Q, Jin Z, Peng T. The microstructure, mechanical properties and creep behavior of Mg–3Sm–0.5Zn–0.4Zr (wt.%) alloy produced by different casting technologies. J Alloy Compd 2010;496:351–6. https://doi.org/10.1016/j.jallcom.2010.01.149.

[19] Ferri TV, Figueiredo AP, Ferreira CRF, Hormaza W, Santos CA, Spim JA. Mechanical properties as a function of microstructure in the new Mg-Al-Ca-La alloy solidified under different conditions. Mater Sci Eng A 2010;527:4624–32. https://doi.org/10.1016/j.msea.2010.03.041.

[20] Kim BH, Jo SM, Lee YC, Park YH, Park IM. Microstructure, tensile properties and creep behavior of Mg–4Al–2Sn containing Ca alloy produced by different casting technologies. Mater Sci Eng A 2012;535:40–7. https://doi.org/10.1016/j.msea.2011.12.038.

[21] Bai J, Sun Y, Xue F, Qiang J. Microstructures and creep properties of Mg-4Al-(1-4) La alloys produced by different casting techniques. Mater Sci Eng A 2012;552:472–80. https://doi.org/10.1016/j.msea.2012.05.072.

[22] Mondal AK, Kesavan AR, Ravi Kiran Reddy B, Dieringa H, Kumar S. Correlation of microstructure and creep behaviour of MRI230D Mg alloy developed by two different casting technologies. Mater Sci Eng A 2015;631:45–51. https://doi.org/10.1016/j.msea.2015.02.037.

[23] Zhao Q, Wu Y, Rong W, Wang K, Yuan L, Heng X. Effect of applied pressure on

microstructures of squeeze cast. J Magnes Alloy 2018;6:197–204. https://doi.org/10.1016/j.jma.2018.04.001.

[24] Manjunath Patel GC, Shettigar AK, Parappagoudar MB. A systematic approach to model and optimize wear behaviour of castings produced by squeeze casting process. J Manuf Process 2018;32:199–212. https://doi.org/10.1016/j.jmapro.2018.02.004.

[25] Lavernia EJ, Srivatsan TS. The rapid solidification processing of materials: science, principles, technology, advances, and applications. J Mater Sci 2010;45:287–325. https://doi.org/10.1007/s10853-009-3995-5.

[26] Barbagallo S, Laukli HI, Lohne O, Cerri E. Divorced eutectic in a HPDC magnesium-aluminum alloy. J Alloys Compd 2004;378:226–32. https://doi.org/10.1016/j.jallcom.2003.11.174.

[27] Nave MD, Dahle AK, StJohn DH. Eutectic growth morphologies in magnesium-aluminium alloys. In: Kaplan HI, Hryn J, Clow B, editors. Magnes. Technol., TMS 2000; 2000, p. 233–42. https://doi.org/10.1002/9781118808962.ch33.

[28] Dantzig JA, Rappaz M. Solidification. EPFL Press; 2009.

[29] Gutman EM, Unigovski Y, Levkovitch M. Influence of porosity and casting conditions on creep of die-cast Mg alloy. J Mater Sci Lett 1998;17:1787–9. https://doi.org/10.1023/A:1006601419020.

[30] Regev M, Aghion E, Rosen A, Bamberger M. Creep studies of coarse-grained AZ91D magnesium castings. Mater Sci Eng A 1998;252:6–16. https://doi.org/10.1016/S0921-5093(98)00668-6.

[31] Wei YH, Hou LF, Yang LJ, Xu BS, Kozuka M, Ichinose H. Microstructures and properties of die casting components with various thicknesses made of AZ91D alloy. J Mater Process Technol 2009;209:3278–84.

https://doi.org/10.1016/j.jmatprotec.2008.07.034.

[32] Dúl J, Szabó R, Simcsák A. Effect of Temperature on the Properties of High Pressure Die Casting. Mater Sci Forum 2010;649:473–9. https://doi.org/10.4028/www.scientific.net/MSF.649.473.

[33] Patel HA, Chen DL, Bhole SD, Sadayappan K. Microstructure and tensile properties of thixomolded magnesium alloys. J Alloys Compd 2010;496:140–8. https://doi.org/10.1016/j.jallcom.2010.02.042.

[34] Nami B, Rashno S, Miresmaeili SM. Effect of tin on the microstructure and impression creep behavior of MRI153 magnesium alloy. J Alloys Compd 2015;639:308–14. https://doi.org/10.1016/j.jallcom.2015.03.109.

[35] Spigarelli S, Regev M, Evangelista E, Rosen A. Review of creep behavior of AZ91 magnesium alloy produced by different technologies. Mater Sci Technol 2001;17:627–38. https://doi.org/10.1179/026708301101510483.

[36] Dieter GE. Mechanical Metallurgy. Third. McGraw-Hill; 2013.

[37] Amberger D, Eisenlohr P, Goken M. On the importance of a connected hard-phase skeleton for the creep resistance of Mg alloys. Acta Mater 2012;60:2277–89. https://doi.org/10.1016/j.actamat.2012.01.017.

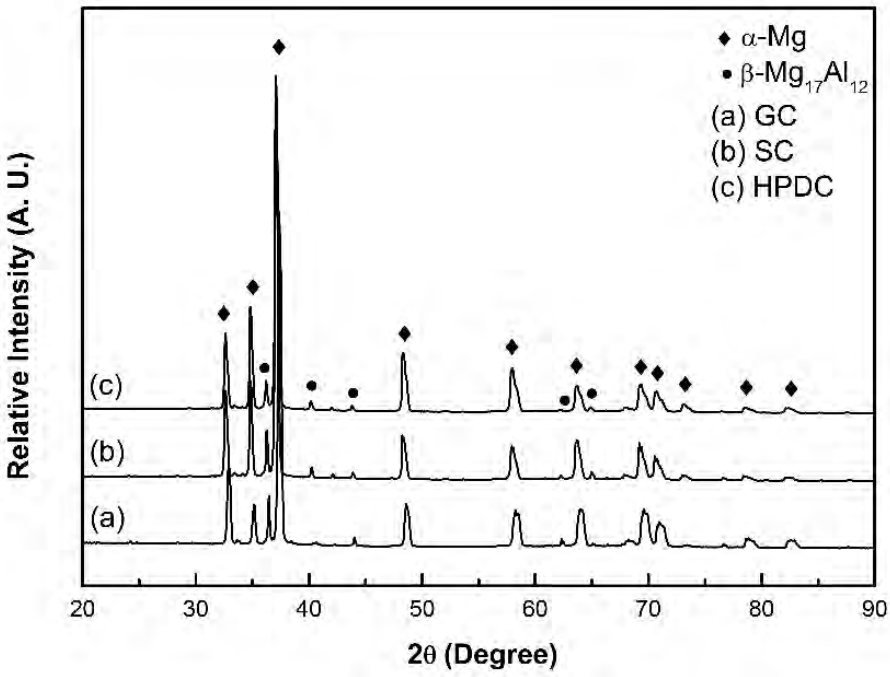

Fig. 1. XRD patterns obtained from the AZ91 alloy in three different casting conditions; gravity casting (GC), squeeze-casting (SC) and high-pressure die-casting (HPDC).

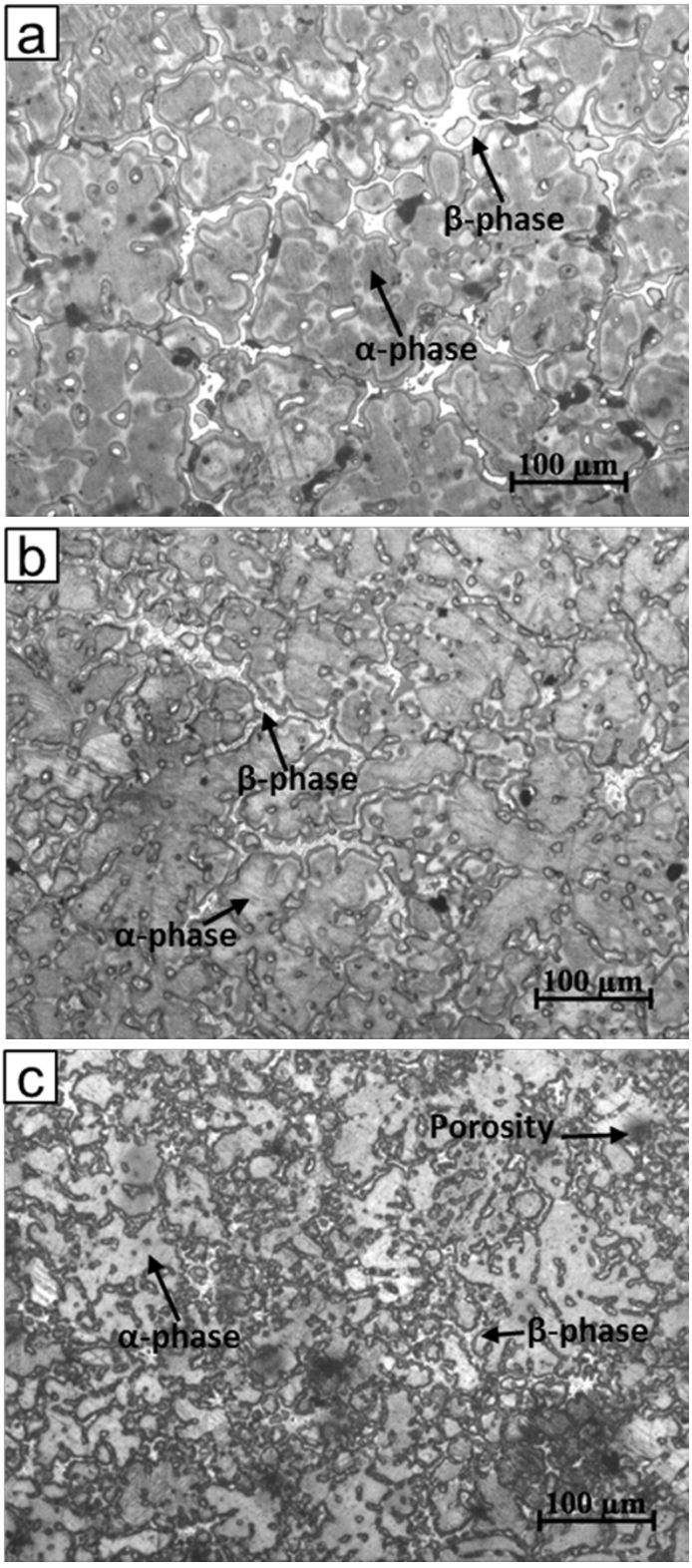

Fig. 2. Optical micrographs of the (a) gravity cast (GC), (b) squeeze-cast (SC) and (c) high-pressure die-casting (HPDC) alloys.

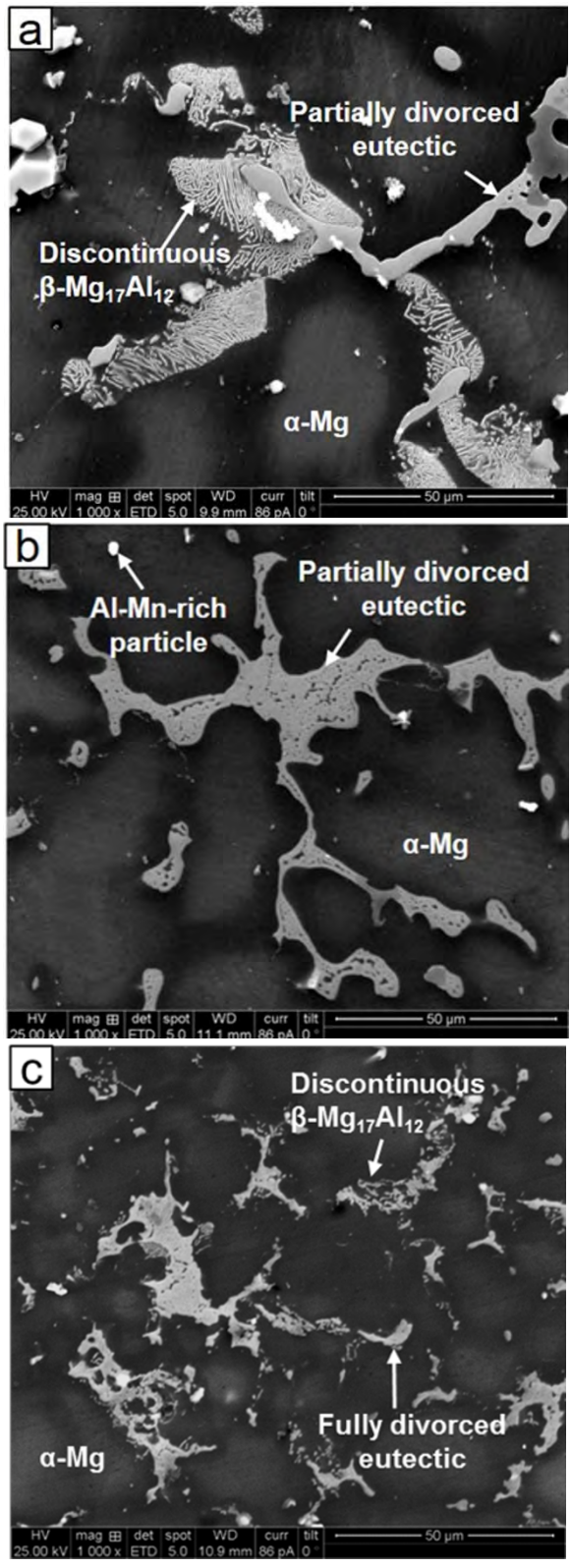

Fig. 3. SEM micrographs of the (a) gravity casting (GC), (b) squeeze-casting (SC) and (c) high-pressure die-casting (HPDC) alloys.

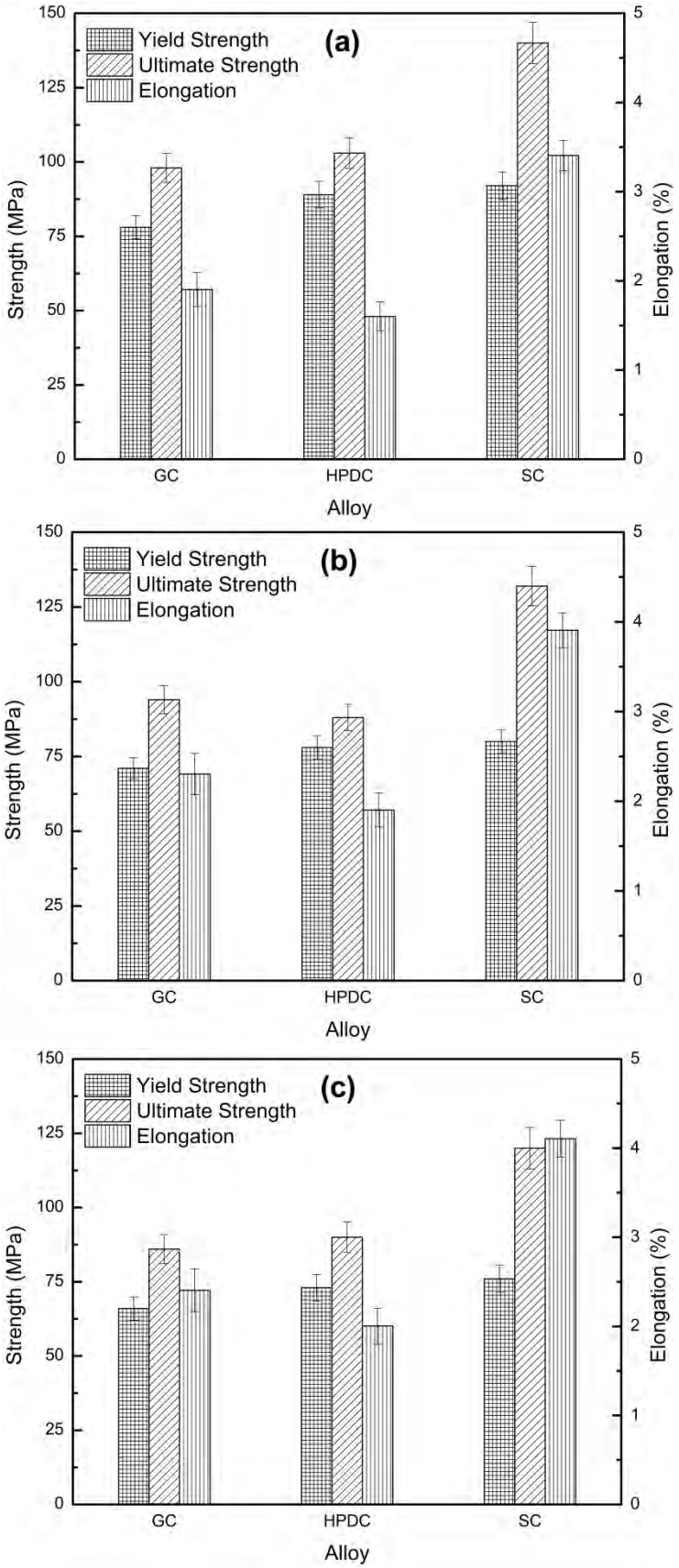

Fig. 4. Comparison of tensile properties of the gravity casting (GC), squeeze-casting (SC) and high-pressure die-casting (HPDC) alloys at (a) ambient, (b) 423 K and (c) 473 K temperature.

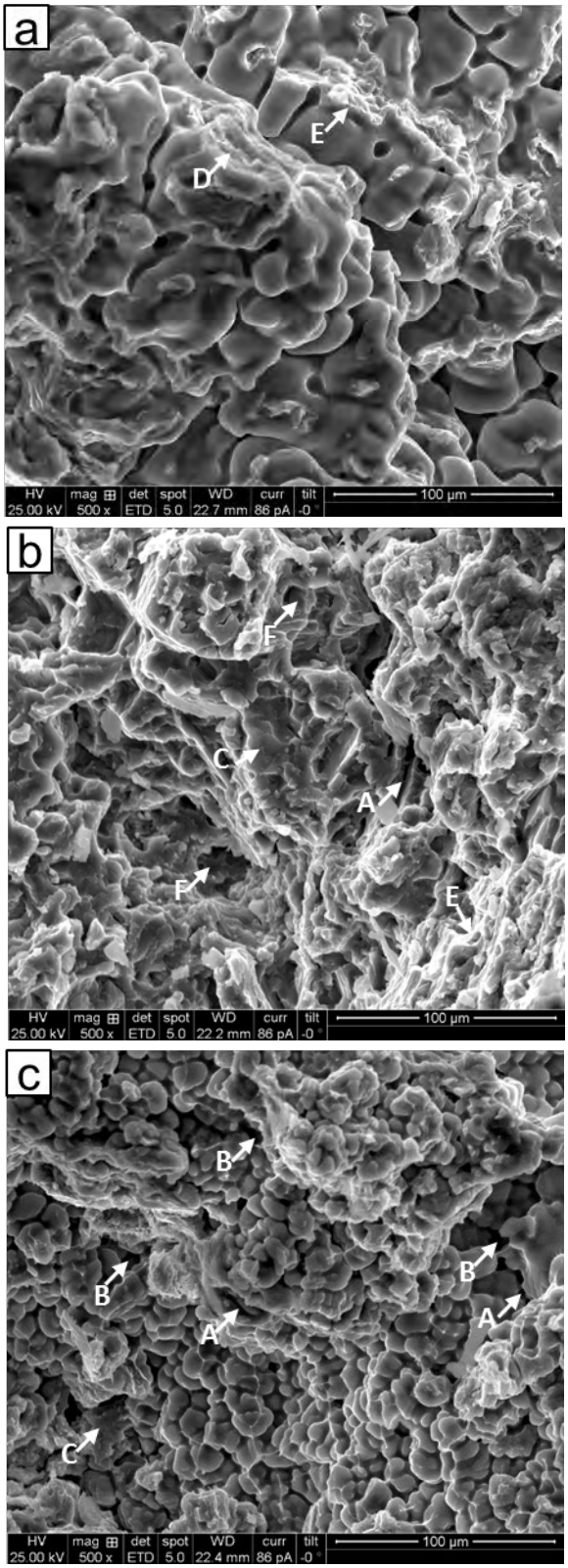

Fig. 5. Fracture surfaces of the tensile specimens of the (a) gravity casting (GC), (b) squeeze-casting (SC) and (c) high-pressure die-casting (HPDC) alloys tested at ambient temperature.

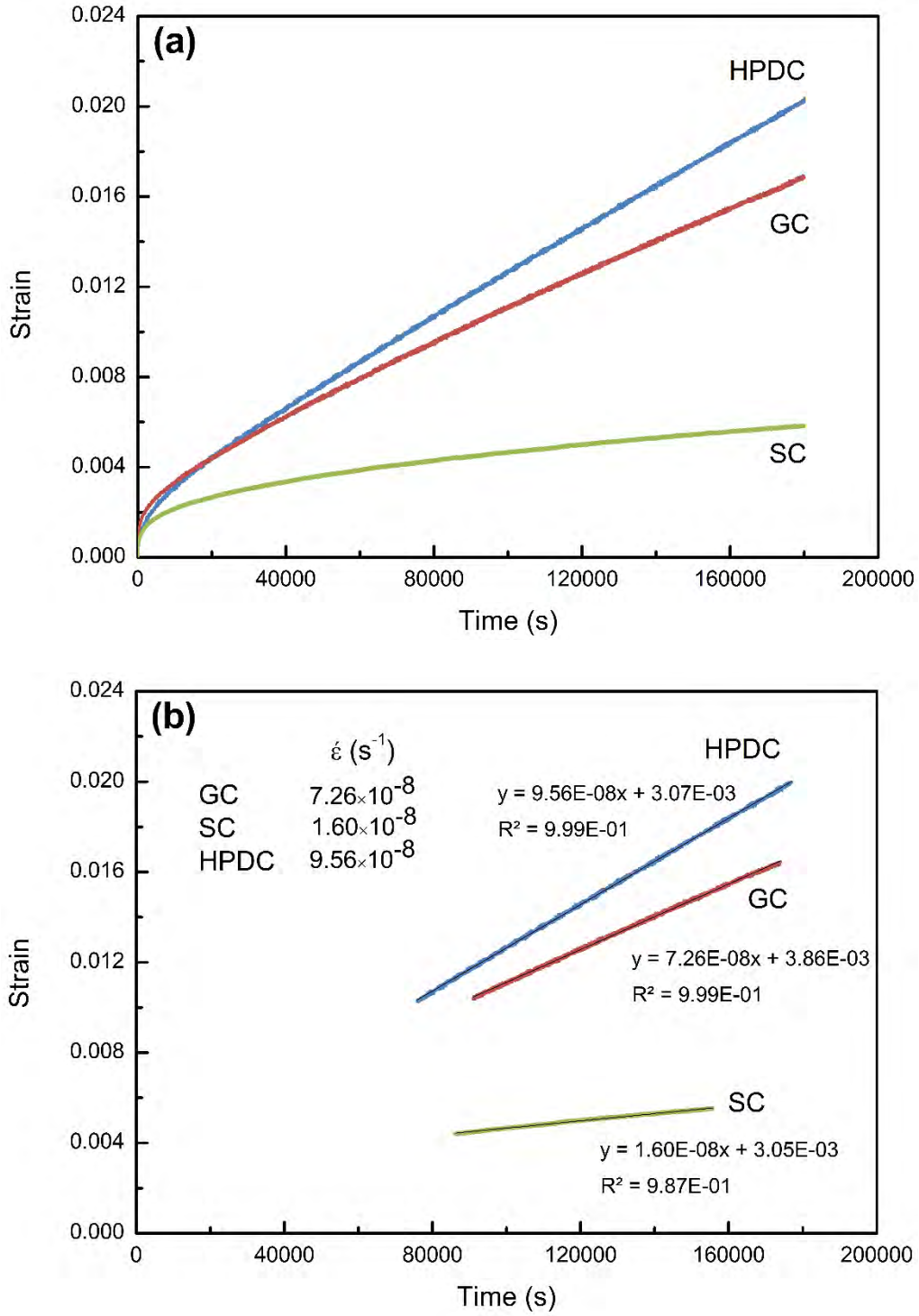

Fig. 6. (a) Strain vs. time plots for the gravity casting (GC), squeeze-casting (SC), and high-pressure die-casting (HPDC) AZ91 alloys creep tested at 70 MPa stress and temperature of 423 K for 50 h, (b) calculation of strain rates by a linear fit to the plots shown in (a).

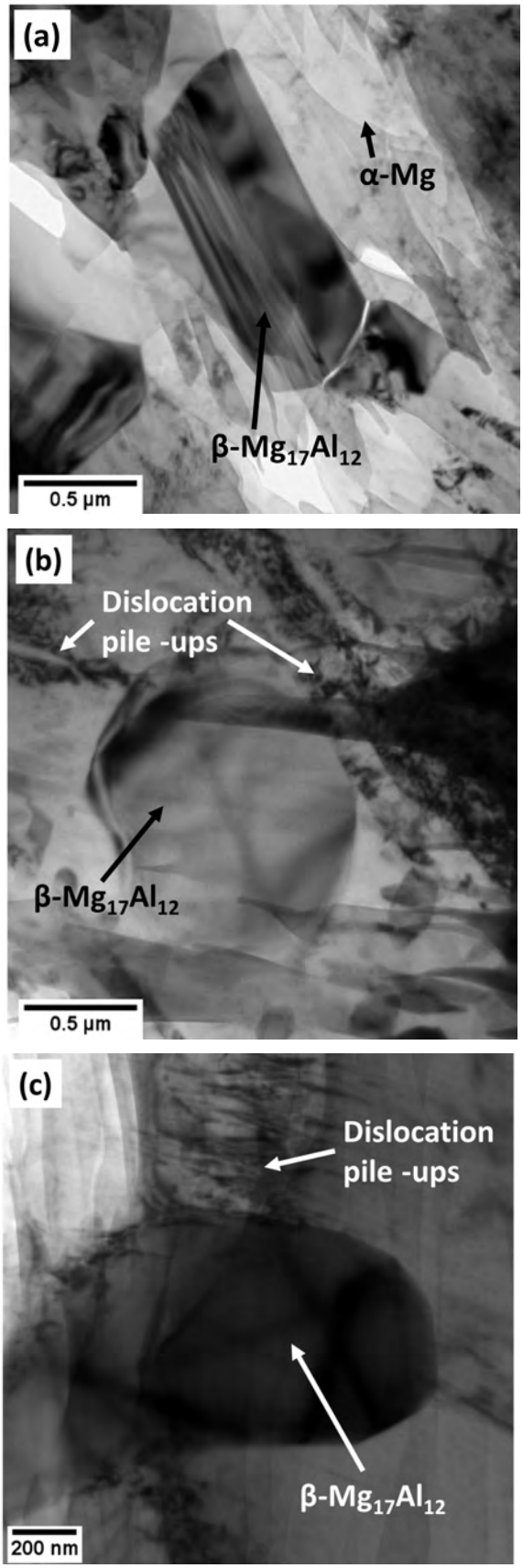

Fig. 7. Bright field TEM micrograph of the squeeze-cast (SC) AZ91 alloy (a) as-cast (before creep test); and (b), (c) after creep tested at 70 MPa and 423 K for 50 h showing dislocations pile-ups near the β-$Mg_{17}Al_{12}$ phase.

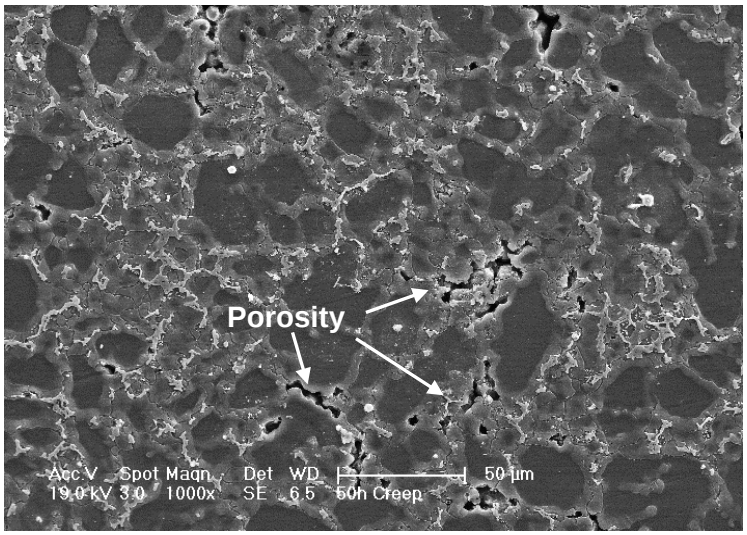

Fig. 8. SEM micrograph of the high-pressure die-casting (HPDC) alloy creep tested at 70 MPa stress and temperature of 423 K for 50 h.